ADVANCED MATERIALS INTERFACES
www.advmatinterfaces.de

Electrical Behaviors of the Co- and Ni-Based POMs Interlayered Schottky Photodetector Devices

Murat Yıldırım, Adem Kocyigit, Yasemin Torlak,* Esma Yenel, Ali Akbar Hussaini, and Mahmut Kuş*

Polyoxometalates (POMs) are attractive materials for various applications such as energy storage, catalysis and medicine. Here, Co and Ni-based POMs are chemically synthesized and characterized by X-ray diffractometer (XRD) and Fourier transform infrared spectroscopies (FT-IR) for structural characterization. While the morphological behaviors are analyzed by scanning electron microscopy (SEM), transmission electron microscopy (TEM) and atomic force microscopy (AFM), the optical properties are investigated by UV-Vis spectrometer. Electrochemical characterizations are carried out by cyclic voltammetry to determine oxidation levels of the metal centers in the POMs. The CoPOM and NiPOM are inserted in between the Al metal and p-Si semiconductor to obtain Al/CoPOM/p-Si and Al/NiPOM/p-Si Schottky-type photodetector devices. Current-voltage (*I–V*) and current-transient (*I–t*) measurements are employed to understand the electrical properties of the Al/CoPOM/p-Si and Al/NiPOM/p-Si devices under dark and various light power intensities. The devices exhibit phototransistor like *I–V* characteristics in forward biases due to having POMs active layers. Various device parameters are extracted from the *I–V* measurements and discussed in details. *I–t* measurements are performed to determine various detector parameters such as responsivity and specific detectivity values for under 2 V and zero biases. The Al/CoPOM/p-Si and Al/NiPOM/p-Si Schottky-type photodetector devices can be employed in optoelectronic applications.

1. Introduction

Polyoxometalates (POMs) are high-oxidation-state transition metal-oxide clusters with a diverse range of properties that render their attractive candidates for a great deal of attention in numerous applications such as energy storage systems,[1] material science,[2] catalysis,[3,4] electrocatalysis,[5] and medicine.[6] They also act as electron acceptors in electrochemical sensors, diodes, and chemical reactions due to their multielectron redox properties and high stability without changing their composition. Some researchers have conducted various studies to improve the light-to-electricity conversion performance of the device by incorporating POMs into semiconductor films.[7,8] During the last few years, POMs have attracted as much attention as photoactive materials due to their rich photochemical activity.[9,10] Since metals within POM clusters have fully oxidized d0 centers, light absorption is generally investigated by O → M ligand to metal charge transfer (LMCT) bands in the range 200–500 nm.[11] When the electron absorbs the photon, a doubly occupied binding orbital (HOMO) forms an oxo-centered radical, and as a result is elevated to the empty, antibonding orbital (LUMO).[12] In addition, different derivatives of photoinduced POM clusters are more reactive compared to other types of clusters in the ground state. Also, they are excellent oxidizing agent (higher electron affinity) and reducing agent (lower ionization energy).[13]

Schottky-type photodiodes or photodetectors are obtained from the metal-semiconductor devices with a thin metallic contact on the top layer.[14] Another way to obtain a Schottky-type

M. Yıldırım, A. A. Hussaini
Department of Biotechnology
Faculty of Science
Selcuk University
Konya 42130, Turkey

A. Kocyigit
Department of Electronics and Automation
Vocational High School
Bilecik Şeyh Edebali University
Bilecik 11230, Turkey
E-mail: adem.kocyigit@bilecik.edu.tr

The ORCID identification number(s) for the author(s) of this article can be found under https://doi.org/10.1002/admi.202102304.

DOI: 10.1002/admi.202102304

Y. Torlak
Cal Vocational High School
Pamukkale University
Denizli 20700, Turkey
E-mail: ytopal@pau.edu.tr

E. Yenel
School of Technical Science
Department of Electricity and Energy
Konya Technical University
Konya 42250, Turkey

M. Kuş
Department of Chemical Engineering
Konya Technical University
Konya 42250, Turkey

photodetector is using a photoactive layer in between the metal and semiconductor with a dot top metallic layer to collect photo-generated electrons.[15] Especially, 2D materials such as graphene and its derivatives have a great interest for fabricating flexible photodetectors and multimode environmental sensors.[16–18] Schottky-type photodetectors have sensitivity to the light, low response time, and good responsivity.[19] There are many studies to improve the light detection performance of these kinds of photodiodes in the literature. Zhang et al. fabricated 2,4-bis[4-(*N*,*N*-dimethylamino)phenyl] squaraine (SQ) nanowire array-based Schottky-type photodetector and obtained better detection performance by using organic layer nanowire arrays.[20] Çiçek et al. obtained non-doped and graphene doped polyvinyl alcohol (PVA) as interfacial layer to improve device performance for Schottky-type junction, and the results confirmed improving performance with increasing graphene doping.[21] Kacus et al. used phenol red as interfacial layer to improve the efficiency of the Co/n-Si Schottky heterostructure, and the results approved good device performance for optoelectronic applications.[22] Wan et al. fabricated self-powered Gr/Si UV photodetector with Al_2O_3 antireflection layer for near-ultraviolet and mid-ultraviolet spectral region, and they achieved fast response time (5 ns), higher internal quantum efficiency than 100%, high photoresponsivity (0.2 AW^{-1}) and specific detectivity (1.6×10^{13} Jones).[23] POMs layers can be employed as photoactive layer between the metal and semiconductor for Schottky-type photodetector.

According to our best knowledge, there are only a few studies on the photodetector application of the POMs layer.[24–26] Our aim is to illuminate the structural, optical, morphological, and electrochemical behaviors of the synthesized $K_7[Co^{III}Co^{II}(H_2O)W_{11}O_{39}].15H_2O$ (CoPOM) and $K_7[Ni^{III}Ni^{II}(H_2O)W_{11}O_{39}].15H_2O$ (NiPOM) compounds, and to employ them for high-performance photodetector applications. In this study, we synthesized and characterized the CoPOM and NiPOM compounds, which have a unique mixed-valence Co(III)/Co(II) and Ni(III)/Ni(II) structural features and are composed of a composition of only earth-abundant elements (cobalt, nickel, tungsten, and oxygen) by various instruments. Then, we employed CoPOM and NiPOM as photoactive layer in between the Al and p-Si for the first time to obtain Schottky-type photodetector devices by *I–V* and *I–t* measurements under dark and various light power intensities.

2. Results and Discussion

2.1. Structural Characterization

X-ray diffraction (XRD) analysis provides very important findings in the identification of the morphological properties of the internal structure of POMs and in the examination of the crystal structure in powder form. XRD patterns of the synthesized CoPOM and NiPOM were recorded and compared, as shown in **Figure 1**a. The diffraction peaks at 25° and 35° in XRD analysis for both POM compounds have dense peaks in this angle range. All observed peaks and their positions are in agreement with previously reported studies related with POMs.[27–29] As seen in Figure 1a, the XRD powder model has

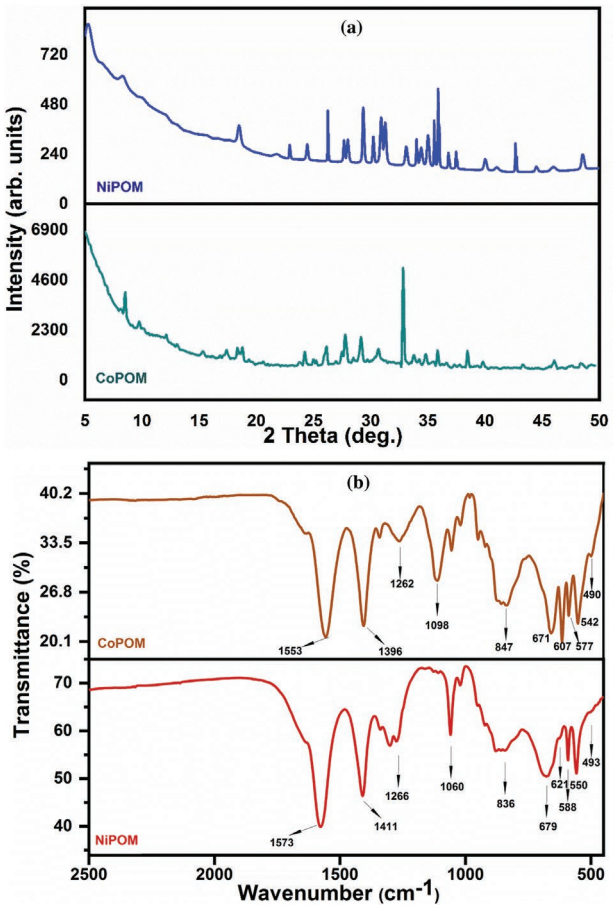

Figure 1. a) XRD powder pattern and b) FT-IR spectra of CoPOM and NiPOM.

high crystallinity, especially at 25–35°, 15–20°, and 35–45° diffractions. The gap crystallinity of these areas is related to POM compounds with Keggin structure containing mixed valance transition metal in their structure.[30–32]

The presence of the heteropolyanion Keggin-type structure with central $Co^{III}O_4$ and $Ni^{III}O_4$ tetrahedron was confirmed for CoPOM and NiPOM by FT-IR technique. Figure 1b reveals FT-IR spectrum of the synthesized CoPOM and NiPOM. The characteristic peaks of the Co–O bending stretching modes of oxygen-metal ions in the tetrahedral regions have values of 1114 (sh) and 825 (s) for CoPOM and 1113 (sh) and 838 (s) for NiPOM. The oxygen-metal ions in the tetrahedral regions, peaks at 659 (s), 615 (m), 586 (w), 548 (w) are assigned to Ni–O bend stretching modes. The peaks at 847 (s), 671 (m), 607 (w), 577 (w) for CoPOM and 836 (s), 679 (m), 621 (w), 588 (w) for NiPOM correspond to the stretching mode of the metal-oxygen bond in the structure.[30] The bands at 1411 and 1573 cm^{-1} for NiPOM, 1396 and 1553 cm^{-1} for CoPOM are due to the presence of water in the sphere of coordination.[33]

2.2. Morphological Characterization

The most versatile and widely used of the technique for the study of the surface characteristic and the morphological

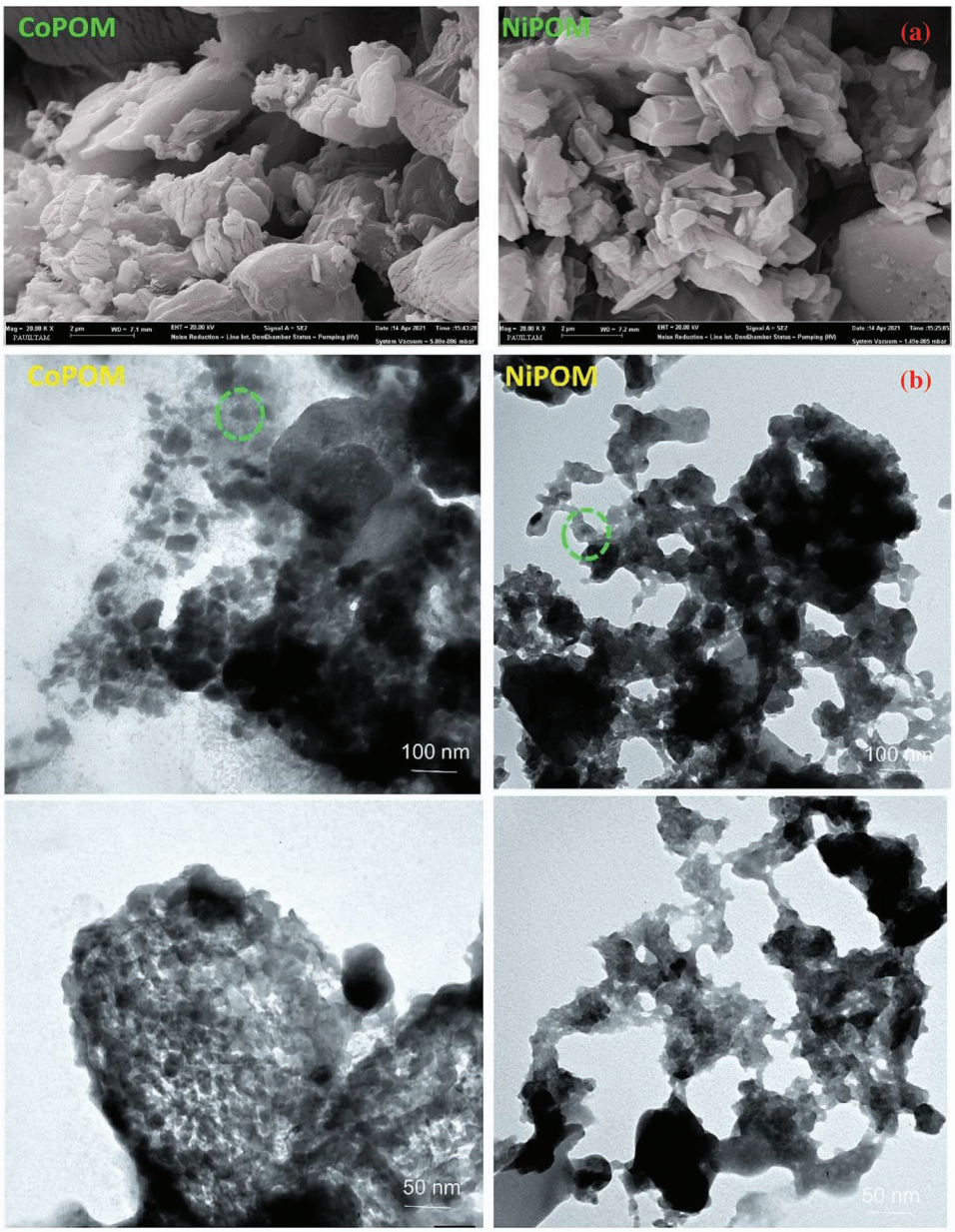

Figure 2. a) SEM images at 20.00 kx magnification and b) TEM images for various magnification of CoPOM and NiPOM.

features of POMs is scanning electron microscopy (SEM). As can be seen from the SEM images of the CoPOM and NiPOM structure in **Figure 2**a, it is clear that the POM nanoparticles are uniformly connected by interacting with each other in networks. Also, they demonstrated a uniform rod-like structure with an average length of about 100–200 nm and a diameter of 30 nm. TEM images are shown in Figure 2b to examine the structural details of the synthesized CoPOM and NiPOM. The particle sizes of POMs are ranging from 50 to 100 nm. The bright-field image of POM particles has shown that the particles are very well dispersed in the polycrystalline shape. However, the particles sometimes tend to aggregate. The bright circle means that there are much more Co and Ni containing POM particles on the surface. This can be interpreted as that the main composition of the shell structures of POM is widely distributed throughout the structure.[34,35] In order to visualize the enhanced surface roughness of the two compounds containing different transition metals, representative AFM images obtained under similar magnifications are examined. Figure S2 (Supporting Information) shows the AFM images of the POMs. The root mean square surface roughness values and average roughness increased from 2.08 and 1.63 nm for NiPOM to 4.07 and 3.25 nm for CoPOM (Figure S2, Supporting Information) due to the structural and transition metal variations. In addition, structure of the POM surface can be observed from 3D AFM image, showing that the distribution of aggregated clusters is almost uniform.

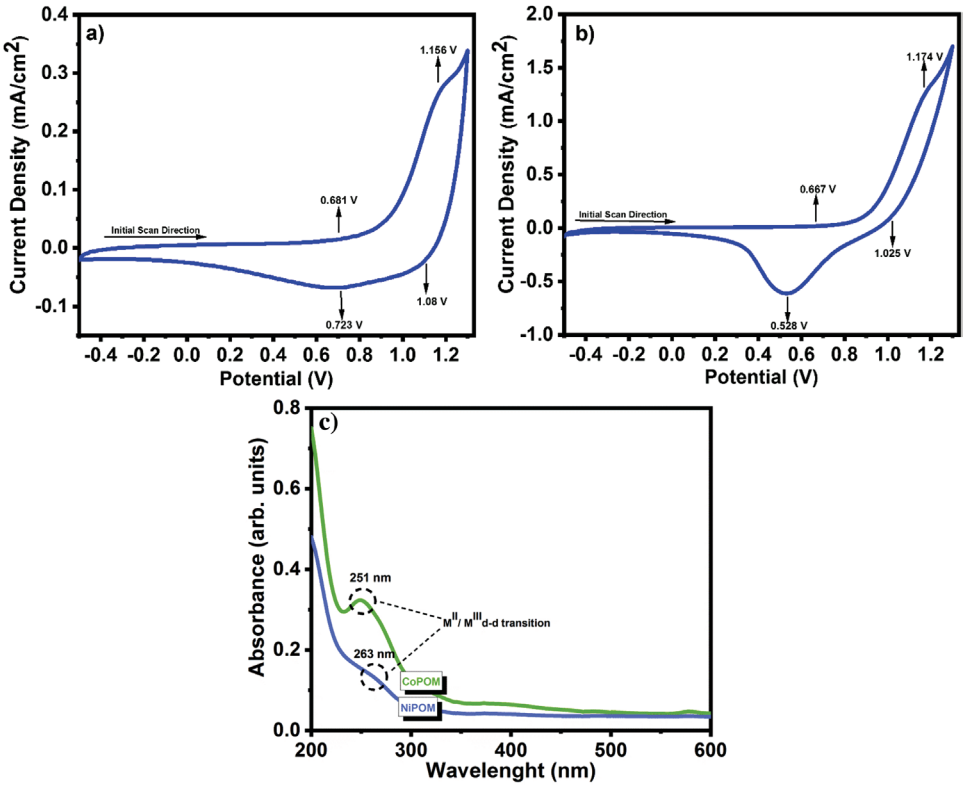

Figure 3. Cyclic voltammogram of a) CoPOM and b) NiPOM on the glassy carbon electrode ([POM] = 1×10^{-3} M in ACN with 0.1 M $TBABF_4$ as supporting electrolyte (Scan rate: 100 mV s^{-1})). c) UV–vis spectra of CoPOM and NiPOM.

2.3. Electrochemical Properties and Optical Characterization of POM Compounds

Cyclic voltammetry is a useful tool to investigate the oxidation levels of the metal centers in the POMs. The redox behaviors of the POMs were carried in acetonitrile (0.1 M $TBABF_4$ solution) by using a glassy carbon working electrode with the potentials referenced to an Ag/AgCl electrode. Two peaks corresponding to metal a Co(III)/Co(II) and Ni(III)/Ni(II) oxidation are clearly observed. The observed potential values indicate that the metal in the low oxidation state is strongly bound to the ligand.[36] CV of CoPOM (the central cobalt valence: +2) and NiPOM (the central nickel valence: +2) indicate two oxidation peaks at around 0.734 and 1.174 ($Co^{II} \rightarrow Co^{III}$), reduction peaks at around 0.674 and 1.036 V according to **Figure 3**a, while oxidation peaks are observed for NiPOM at around 0.645 and 1.156 ($Ni^{II} \rightarrow Ni^{III}$) and reduction peaks at around 0.524 and 0.972 according to Figure 3b.[37] CoPOM modified electrode showed a pair of redox peaks with oxidation peak of $Co^{II} \rightarrow Co^{III}$ at about 0.681 V and oxidation peak of $Co^{III} \rightarrow Co^{IV}$ at about 1.08 V. NiPOM modified electrode showed a pair of redox peaks with oxidation peak of $Ni^{II} \rightarrow Ni^{III}$ at about 0.667 V and oxidation peak of $Ni^{III} \rightarrow Ni^{IV}$ at about 1.02 V.

Absorbance spectra of POM solutions in water are measured at pH:7.0 and given in Figure 3c. Two absorption peaks at 251 nm and 263 nm wavelengths are observed for POMs which are in agreement with the literature.[38,39] Since CoPOM contains both Co(II) and Co(III) centers and NiPOM contains both Ni(II) and Ni(III) centers, the band at 251 and 263 nm is assigned as a d–d transition of the Co(III) and Ni(III) center.[40] In addition, the ligand-to-metal charge transfer (LMCT) band has been seen at 251 nm for CoPOM compound and 263 nm for NiPOM compound. The Co^{III} center in CoPOM and Ni^{III} in NiPOM contribute to the stability of the Dawson-type polyanionic structure.[41]

2.4. Electrical Characteristics of the Al/CoPOM/p-Si and Al/NiPOM/p-Si Photodiodes

I–V characteristics of the Al/CoPOM/p-Si and Al/NiPOM/p-Si devices have been shown in Figure S3a,b (Supporting Information) for various light power intensities, respectively. Both the Al/CoPOM/p-Si and Al/NiPOM/p-Si devices exhibited increasing current profile in the forward bias region with increasing light power intensity. The Al/CoPOM/p-Si and Al/NiPOM/p-Si devices can be thought as two-lead phototransistors due to exhibiting a phototransistor behavior and increasing base current with increasing light power intensity and staying constant with increasing voltage in the forward bias region. However, in the case of the Al/CoPOM/p-Si device, the photocurrent increased with increasing light power and voltage almost linearly. The phototransistors usually are fabricated on the SiO_2/Si surface as FET structure or PNP structure as BJT on a one substrate and they are illuminated for switching.[42–45] In our study, we used normal Schottky-type photodetector structure with n-type POM interlayers. The devices clearly behaved such a phototransistor of BJT due to the forming the

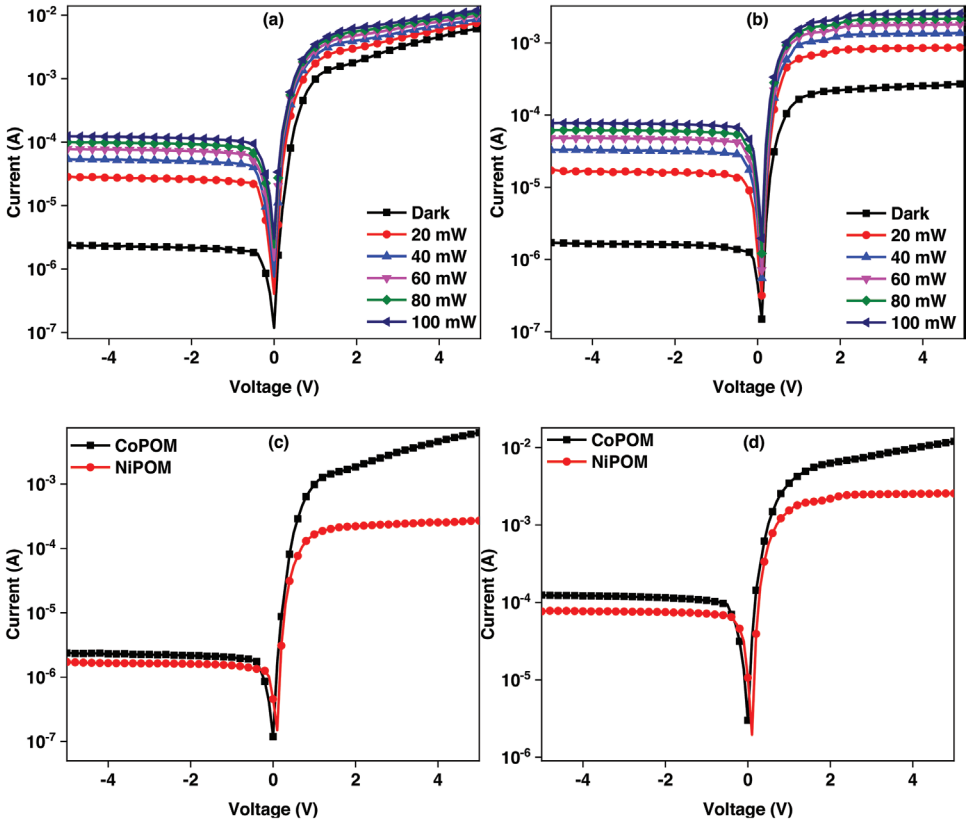

Figure 4. ln *I–V* plots of the a) Al/CoPOM/p-Si and b) Al/NiPOM/p-Si devices. Comparison *I–V* characteristics of the Al/CoPOM/p-Si and Al/NiPOM/p-Si photodiodes c) dark and d) 100 mW cm^{-2} light intensity.

PNP type transistor in the forward bias as shown in the inset of Figure S3b (Supporting Information). The n-type CoPOM and NiPOM layers can absorb the light and emit electrons to the medium.[46] While the photodiodes or photodetectors work in the reverse biases, the phototransistors run in the forward bias region. We have both photodiode behavior in reverse biases and phototransistor behavior in the forward bias region. The threshold or knee voltage values of the Al/CoPOM/p-Si and Al/NiPOM/p-Si devices were calculated from these graphs and discussed in the next sections.

ln *I–V* plots can help to calculate ideality factor, and barrier height as well as series resistance of the metal-semiconductor devices by the most widely used techniques such as thermionic emission theory, Norde and Cheung methods.[47] According to thermionic emission theory, while the slope of the second region at the forward bias ln *I–V* plot provides to calculate the ideality factor, *y*-intercept of the plot helps calculate barrier height value.[48] **Figure 4**a,b show the ln *I–V* plots of the Al/CoPOM/p-Si and Al/NiPOM/p-Si devices depending on the increasing light power. The changes of the current in the reverse bias regions can clearly be seen in those graphs. Both devices exhibited increasing photocurrent profile in the reverse bias as well as forward bias regions. This result highlighted the photodiode behavior of the fabricated devices with phototransistor behaviors.[49] The currents increased almost more than at least 10 folds for both devices. ln *I–V* characteristics of both devices were plotted together to compare the reaction of the Al/CoPOM/p-Si and Al/NiPOM/p-Si devices in dark and 100 mW cm^{-2} light power. Figure 4c, displays ln *I–V* characteristics of the Al/CoPOM/p-Si and Al/NiPOM/p-Si devices under dark and 100 mW cm^{-2} light power intensity. The Al/NiPOM/p-Si photodiode has low reverse and forward bias currents in the dark and 100 mW cm^{-2} light power intensity. However, the stability of the current at the Al/NiPOM/p-Si is better than the Al/CoPOM/p-Si device especially in forward biases.

The ideality factor (n), saturation current (I_0) and barrier height values (Φ_b) were calculated and listed in **Table 1** according to thermionic emission theory for dark condition. The

Table 1. Various diode parameters for the Al/CoPOM/p-Si and Al/NiPOM/p-Si devices.

Interface type	Saturation current I_0 (10^{-7} A)	n (*I–V*)	n Cheung	Φ_b (*I–V*) [eV]	Φ_b Cheung [eV]	Φ_b Norde [eV]	R_s Cheung [kΩ ($H(I)$)]	R_s Cheung [kΩ ($dln(I)$)]	R_s Norde [kΩ]
CoPOM	6.09	3.02	3.37	0.63	0.61	0.68	0.42	0.51	0.31
NiPOM	4.66	3.34	3.26	0.64	0.62	0.67	3.26	3.12	1.23

ideality factor values of the Al/CoPOM/p-Si and Al/NiPOM/p-Si devices were determined as 3.02 and 3.34, and the barrier height values were calculated as 0.63 and 0.64 eV, respectively. The high ideality factor values at the Al/CoPOM/p-Si and Al/NiPOM/p-Si devices can be attributed to barrier inhomogeneity and interfacial POM layers as well as series resistance rather than more than unity.[50,51]

The threshold voltages of the Al/CoPOM/p-Si and Al/NiPOM/p-Si devices were determined as 0.38 and 0.25 V under dark, respectively. The threshold voltage changes with changing light power have been shown in Figure S4a (Supporting Information). The threshold voltage values decreased slightly with increasing light power for the Al/CoPOM/p-Si and Al/NiPOM/p-Si devices. However, the Al/NiPOM/p-Si device has lower threshold voltage changes. These threshold voltage values are in good agreement for Si-based Schottky-type devices.[52] Moreover, the ideality factor, barrier height, and rectifying ratio (RR) values for changing light power intensity were calculated for the Al/CoPOM/p-Si and Al/NiPOM/p-Si devices. The light power-dependent profile of the ideality factor, barrier height, and rectifying ratio have been indicated in Figure S4b–d (Supporting Information), respectively. While the ideality factor values generally increased with increasing light power intensity, barrier heights and rectifying ratio values decreased for the Al/CoPOM/p-Si and Al/NiPOM/p-Si devices. The increasing of the ideality factor values and decreasing of the barrier height values with increasing light power intensity can be attributed to increasing charge carriers in the interface of the devices or increasing photocurrent at the forward biases. In the case of RR values, the decrease can be attributed to the increasing rate of the reverse bias photocurrent with increasing light power intensity more than forward biases.

The series (R_s) and shunt resistance (R_{sh}) values can be extracted from the *I–V* characteristics by the plotting of the junction resistance (R_j) depending on the changing voltage. While the reverse bias region of the R_j shows R_{sh}, forward bias region of the R_j indicates R_s of Schottky-type devices.[47] R_j versus voltage plots were used to calculate the R_{sh} and R_s values (data not shown here). The Al/CoPOM/p-Si photodiode has R_{sh} at around 8–10 MΩ and R_s at about 18 kΩ. In the case of the Al/NiPOM/p-Si photodiode, the R_{sh} value is 25–600 MΩ and R_s value is about 50–100 kΩ.

The device parameters were calculated by Cheung and Norde method to confirm the calculated parameters from the thermionic emission theory.[53–55] While **Figure 5**a,b shows the Cheung plots of the Al/CoPOM/p-Si and Al/NiPOM/p-Si devices, Figure 5c,d indicates the Norde plots of the Al/CoPOM/p-Si and Al/NiPOM/p-Si photodiodes, respectively. The calculated device parameters have been given in Table 1. The obtained device parameters are in good harmony with each other. The small differences of the device parameters can be attributed to approximation differences.[56] The obtained series resistance values of the Al/CoPOM/p-Si are lower than the Al/NiPOM/p-Si device.

Current transient (*I–t*) measurements of the Al/CoPOM/p-Si and Al/NiPOM/p-Si devices have been shown in Figure S5a,b (Supporting Information), respectively depending on the light power intensity. The currents of the Al/CoPOM/p-Si and

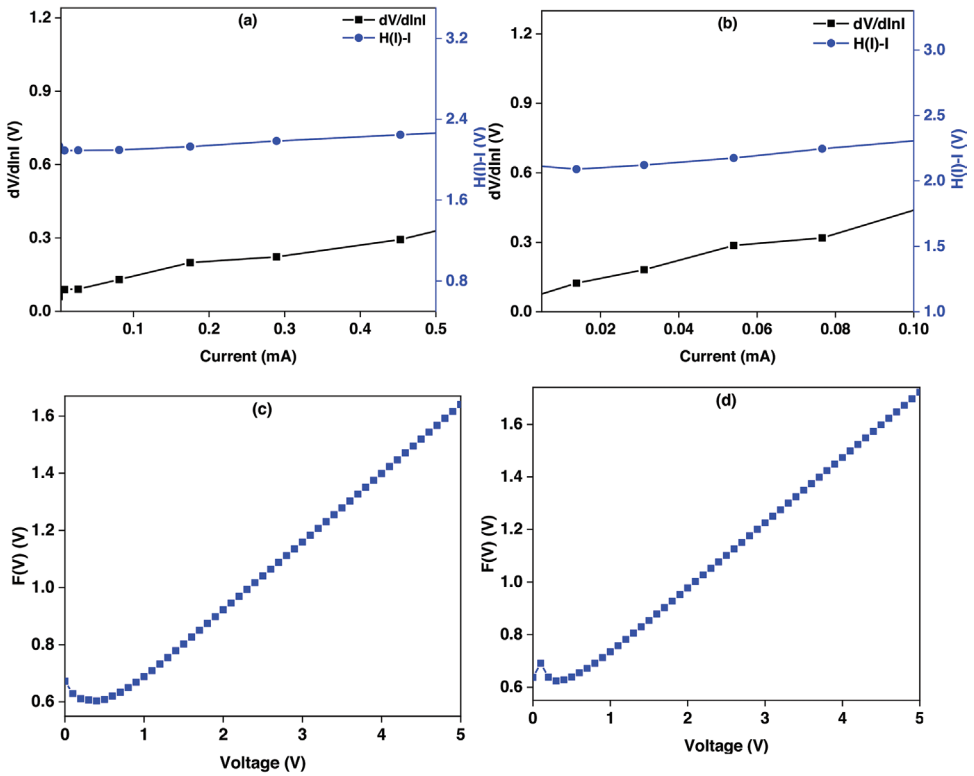

Figure 5. Cheung plots of the a) Al/CoPOM/p-Si and b) Al/NiPOM/p-Si photodiodes. *F(V)–V* plots of the c) Al/CoPOM/p-Si and d) Al/NiPOM/p-Si devices.

Al/NiPOM/p-Si devices suddenly increased when the light is on, and decreased immediately when the light is off position for all various light power intensity values. This result highlighted that the fabricated devices have good responsivity to the light illumination.[57] Moreover, the current increased almost linearly on both the Al/CoPOM/p-Si and Al/NiPOM/p-Si devices with increasing light power intensity and maximum current were obtained for 100 mW cm^{-2} values. The rise and fall times of the devices were obtained as 800 ms for both the Al/CoPOM/p-Si and Al/NiPOM/p-Si devices (in Figure S6a,b, Supporting Information). These results implied good response time according to literature.[58]

The data from *I–t* graphs were used to calculate various photodetector parameters such as photocurrent, photosensitivity, responsivity, specific detectivity, and noise equivalent power. Their formulas are given in equations from (1) to (5).[59] The I_p shows photocurrent, *K* exhibits photosensitivity, *R* represents responsivity, *D** indicates specific detectivity, and NEP is noise equivalent power or detectivity limit.[60,61]

$$I_{\mathrm{p}} = I_{\mathrm{light}} - I_{\mathrm{dark}} \tag{1}$$

$$K = \frac{I_{\mathrm{p}}}{I_{\mathrm{dark}}} \tag{2}$$

$$R = \frac{I_{\mathrm{p}}}{PA} \tag{3}$$

$$D^{*} = R\sqrt{\frac{A}{2qI_{\mathrm{dark}}}} \tag{4}$$

$$NEP = \frac{\sqrt{A\Delta f}}{D^{*}} \tag{5}$$

Here *q* is the charge of the electron, *A* is detector area, and Δf is bandwidth.

Various photodetector parameters of the Al/CoPOM/p-Si and Al/NiPOM/p-Si devices were calculated and listed in **Table 2** for changing light power intensity. While the photocurrent and photosensitivity values increased linearly with increasing light power, responsivity and specific detectivity values decreased exponentially according to Table 2. The obtained responsivity values are good enough for a Schottky-type photodiode. Both the obtained responsivity and specific detectivity values are high according to a kind of Schottky-type photodetector without any graphene layer, and the devices can be employed optoelectronic applications.[62]

The polyoxometalates have been rarely used for improving of the performances of the photodetectors in the literature. Li et al. studied photoconductivity of Keggin-type tungsten-series POMs for potential application in sensors, photodetectors, and photocatalysis, and they concluded that the POMs exhibited good photoconductivity.[26] Xie et al. operated Keplerate-type POM with polyethyleneimine to obtain $CH_3NH_3PbI_3$ based perovskite composite photodetector, and they reached 6.02 mA W^{-1} responsivity values under sun radiation.[63] Xu et al. used $CH_3NH_3PbI_3$ perovskite with graphitic carbon nitride (g-C_3N_4) with POM layer to increase photocurrent 2.6 times by increasing grain size, decreasing passivating defect states (with g-C_3N_4) and improving light absorption (with POM layer).[64] Zheng et al. employed POM for ZnO nanowire photodetector for improving the UV absorption of the ZnO nanowires by 36.9%. They also obtained high responsivity and detectivity values by this POM-modified ZnO nanowire photodetector.[65] Furthermore, the results of the Al/CoPOM/p-Si and Al/NiPOM/p-Si photodetectors have been compared with recent literature in **Table 3** for other types of materials in the case of photodetector applications. According to Table 3, the obtained responsivity, specific detectivity and photosensitivity values of Al/CoPOM/p-Si and Al/NiPOM/p-Si photodetectors are good agreement with literature for various materials.

To determine detectivity, responsivity, photosensitivity, and detection limit values at zero bias are important to evaluate the performance of a photodetector because these kinds of photodetectors can be used in low power consumptions applications such as wearable devices, internet of things.[66] Zero bias detector parameters have been listed in Table S1 (Supporting Information) for the Al/CoPOM/p-Si and Al/NiPOM/p-Si devices. While the photosensitivity, responsivity and specific

Table 2. Various photodetector parameters of the Al/CoPOM/p-Si and Al/NiPOM/p-Si devices depending on the light power intensity under 2 V bias.

Photodetector	Power [mW cm^{-2}]	I_p [A]	*K* [–]	*R* [A W^{-1}]	*D** [Jones]	NEP [W $Hz^{-1/2}$]
Al/CoPOM/p-Si	20	1.16×10^{-3}	0.72	7.38	2.88×10^{10}	3.07×10^{-12}
	40	1.95×10^{-3}	1.18	6.20	2.39×10^{10}	3.70×10^{-12}
	60	2.72×10^{-3}	1.60	5.77	2.19×10^{10}	4.04×10^{-12}
	80	3.38×10^{-3}	1.95	5.38	2.03×10^{10}	4.37×10^{-12}
	100	4.03×10^{-3}	2.28	5.13	1.91×10^{10}	4.64×10^{-12}
Al/NiPOM/p-Si	20	6.54×10^{-4}	4.61	4.16	5.48×10^{10}	1.62×10^{-12}
	40	1.09×10^{-3}	7.54	3.49	4.53×10^{10}	1.96×10^{-12}
	60	1.48×10^{-3}	9.94	3.14	4.03×10^{10}	2.20×10^{-12}
	80	1.77×10^{-3}	11.57	2.81	3.57×10^{10}	2.49×10^{-12}
	100	2.06×10^{-3}	13.04	2.63	3.27×10^{10}	2.71×10^{-12}

Table 3. The comparison of the Al/CoPOM/p-Si and Al/NiPOM/p-Si photodetectors with some recently published works.

Device	Device type	Wavelength [nm]	Photosensitivity [–]	Responsivity [A W^{-1}]	Detectivity [Jones]	Refs.
Pd/Bi_2O_2Se/Ti	MSM	500	–	193.00	7.00×10^{11}	[70]
Al/CuAlMn/n-Si/Al	Schottky diode	365	5.55	0.14	1.21×10^{10}	[71]
$MoTe_2$-WS_2- $MoTe_2$	Avalanche photodiode	400–700	–	6.02	6.47×10^{10}	[72]
Cu/ZnO/Cu	MSM	365	–	1.20	5.77×10^{11}	[73]
Cu/Yb@V_2O_5/n-Si	Schottky diode	–	55.45	0.04	9.97×10^{10}	[74]
p-type BP-FL/Al	Schottky diode	Solar radiation	–	0.01	7.49×10^{7}	[75]
Au/Ni/Si-doped β-Ga_2O_3/Ti/Au	MSM	254	–	366.88	2.33×10^{13}	[76]
Au/NTCDA/p-Si/Al	Schottky diode	194	–	0.02	1.50×10^{10}	[77]
(c-ITO)/native SiO_x/n-Si	Schottky diode	880	–	0.55	2.14×10^{13}	[78]
Cr/Au/GeAs/Cr/Au	MSM	660	–	905.50	8.60×10^{12}	[79]
Al/WPOM/p-Si and Al/MoPOM/p-Si	Schottky diode	Solar radiation	103.15	1.87	8.38×10^{11}	[24]
FG on GR-FG/Si	MSM	200 to 1100 nm	–	0.50	7.40×10^{9}	[80]
GR/ultrathin Si	MSM	UV region	–	0.47	2.50×10^{10}	[81]
Al/CoPOM/p-Si and Al/NiPOM/p-Si	Schottky diode	Solar radiation	13.04	7.38	5.48×10^{10}	This work

detectivity values increased with increasing light power, detection limit decreased for Al/CoPOM/p-Si and Al/NiPOM/p-Si devices. These results confirmed that Al/CoPOM/p-Si and Al/NiPOM/p-Si devices can be employed self-powered photodetector.[67]

3. Conclusion

Co and Ni-based polyoxometalates (POMs) were synthesized successfully chemically and characterized by various instruments. XRD results revealed that CoPOM and NiPOM have crystalline structure in nature. FT-IR results showed the various bond structures of the CoPOM and NiPOM structures. Morphological characterization by SEM, TEM, and AFM indicated that the CoPOM and NiPOM structures have uniform rod-like particles with 50–100 nm dimensions. UV–Vis spectrometer results clearly exhibited the absorbance peaks of the CoPOM and NiPOM structures. Cyclic voltammetry results confirmed the oxidation level of the metal centers. The electrical characterization of the Al/CoPOM/p-Si and Al/NiPOM/p-Si devices was performed by *I–V* measurements under dark and various light power intensities and, the results were discussed and compared to each other in detail. Various device parameters from *I–V* measurements and detector parameters from the *I–t* measurements were extracted. The devices exhibited high responsivity and specific detectivity. The overall results highlighted those POMs layers are quite proper materials for optic communication, safety, and environmental sensing applications.

4. Experimental Section

Synthesis of CoPOM ($K_7[Co^{III}Co^{II}(H_2O)W_{11}O_{39}].15H_2O$): The chemicals required for the synthesis of CoPOM and NiPOM ($Na_2WO_4{\cdot}2H_2O$, $Co(OAc)_2{\cdot}4H_2O$, $Ni(OAc)_2{\cdot}4H_2O$, $K_2S_2O_8$ and KNO_3) were purchased from Sigma-Aldrich and used without purification. A mixture of $Na_2WO_4{\cdot}2H_2O$ (0.06 mmol) in 40 mL water was stirred at room temperature for 2 h and heated to reflux for 3 h under argon atmosphere. Then, a 4 mL of glacial acetic acid was added, and the pH value of this mixture was adjusted to the range of 6–7. In order to make sure the reaction to be controlled, $Co(OAc)_2{\cdot}4H_2O$ (0.01 mol) was dissolved in 13 mL of ultrapure water and added dropwise into the mixture. A 7 g of $K_2S_2O_8$ was slowly added to the solution after reaching 80 °C temperature. When the color of the solution turns from dark green to brown, KNO_3 was added. The solution was adjusted to room temperature, and the obtained brown solid obtained by this process was filtered.[38]

Synthesis of NiPOM ($K_7[Ni^{III}Ni^{II}(H_2O)W_{11}O_{39}]{\cdot}\ 15H_2O$): The NiPOM compound was prepared according to the same procedure as the CoPOM compound. A mixture of $Na_2WO_4{\cdot}2H_2O$ (0.06 mmol) in 40 mL water was stirred at room temperature for 2 h and heated to reflux for 3 h under argon atmosphere. Later, a 4 mL of glacial acetic acid was added, and the pH value of this mixture was adjusted to the range of 6–7. In order to control the reaction, $Ni(OAc)_2{\cdot}4H_2O$ (0.01 mol) was dissolved in 13 mL of ultrapure water and added dropwise to the mixture. A 7 g of $K_2S_2O_8$ was slowly added into the solution after reaching 80 °C. When the color of the solution turns from dark green to brown, KNO_3 was added. The solution was adjusted to room temperature, and the obtained green solid obtained by this process was filtered.[38]

Fabrication of the CoPOM and NiPOM Interlayered Photodiodes: The fabrication processes of the Al/CoPOM/p-Si and Al/NiPOM/p-Si photodetectors were started with the cleaning of the p-Si wafer, which had (100) crystal orientation, 1–10 Ω cm resistivity and 300 µm thicknesses, as substrate and semiconductor material. The silicon wafer was cut into 2 cm^2 square pieces and cleaned by ultrasonic cleaner in acetone, distilled water, and isopropanol for 30 min. Then, the wafer pieces were immersed into HF:H_2O (1:10) solution to remove native oxide layers from the Si surfaces for 30 s. These pieces, then, were immediately transferred into thermal evaporator in MBRAUN glove box platform to obtain Al ohmic contact on the back surfaces with the thickness of 100 nm. The obtained CoPOM and NiPOM solutions were coated on the front or polished surfaces by spin coating technique at 3000 rpm and in 30 s. The CoPOM and NiPOM layers were heated up on a heater at 80 °C, and then they were transferred the thermal evaporator chamber to achieve Al metallic contact on the top of CoPOM and NiPOM layers. Thus, the Al/CoPOM/p-Si and Al/NiPOM/p-Si photodetectors were successfully fabricated. The schematic and band

diagrams of the photodetectors with heteropolyanion Keggin-type structure of the POM layers has been shown in Figure S1a,b (Supporting Information), respectively.[68] When theoretically two Schottky junctions have symmetrical design, the device cannot exhibit photocurrent at zero biases for that reason. The symmetry should be broken for effective photodetectors by adding an interfacial layer between metal and semiconductor, using asymmetrical metallic contacts or choosing different contact that have different work functions. One used as interlayer of CoPOM and NiPOM for that reason.[69]

Characterization: In the range 400–4000 cm^{-1}, the FT-IR spectrum of POMs was recorded at room temperature on Bruker Vertex 70 model spectrophotometer. UV–vis absorption spectra were recorded on an Agilent 8453 UV–Vis spectrophotometer. The powder XRD pattern was collected with a PANalytical Empyrean using Cu-Kα radiation. Cyclic voltammogram measurements were performed on an Ivium Compactstat instrument by using glassy carbon as the working electrode, an Ag wire as the reference electrode, and a Pt wire as the counter electrode. For the further evaluation, surface morphologies and topographies of the POMs were characterized using a scanning electron microscopy (SEM, Zeiss EVOLS10), transmission electron microscopy (TEM, JEOL JEM-1400Flash) and atomic force microscopy (AFM, NT-MDT Ntegra). The *I–V* and *I–t* measurements were performed to characterize the Al/CoPOM/p-Si and Al/NiPOM/p-Si photodiodes by Fytronix FY-7000 instruments under dark and various light intensities of 20–100 mW cm^{-2}.

Supporting Information

Supporting Information is available from the Wiley Online Library or from the author.

Acknowledgements

This work was supported by Selçuk University BAP office with the research Project Number of 21401060.

Conflict of Interest

The authors declare no conflict of interest.

Data Availability Statement

Research data are not shared.

Keywords

optoelectronic applications, photodiodes, polyoxometalates, Schottky-type photodetectors

Received: November 24, 2021
Revised: April 8, 2022
Published online: May 20, 2022

[1] S. Herrmann, N. Aydemir, F. Nägele, D. Fantauzzi, T. Jacob, J. Travas-Sejdic, C. Streb, *Adv. Funct. Mater.* **2017**, *27*, 1700881.
[2] Y. Wang, I. A. Weinstock, *Chem. Soc. Rev.* **2012**, *41*, 7479.
[3] X.-S. Wang, Y.-B. Huang, Z.-J. Lin, R. Cao, *Dalton Trans.* **2014**, *43*, 11950.
[4] S. Zhang, Y. Lu, X.-W. Sun, Z. Li, T.-Y. Dang, Z. Zhang, H.-R. Tian, S.-X. Liu, *Chem. Commun.* **2020**, *56*, 391.
[5] V. Singh, S. D. Adhikary, A. Tiwari, D. Mandal, T. C. Nagaiah, *Chem. Mater.* **2017**, *29*, 4253.
[6] J. T. Rhule, C. L. Hill, D. A. Judd, R. F. Schinazi, *Chem. Rev.* **1998**, *98*, 327.
[7] Y. Zhang, R. Tao, X. Zhao, Z. Sun, Y. Wang, L. Xu, *Chem. Commun.* **2016**, *52*, 3304.
[8] W. Li, G. Jin, H. Hu, J. Li, Y. Yang, Q. Chen, *Electrochim. Acta* **2015**, *153*, 499.
[9] T. Yamase, *Chem. Rev.* **1998**, *98*, 307.
[10] C. Streb, *Dalton Trans.* **2012**, *41*, 1651.
[11] E. Papaconstantinou, *Chem. Soc. Rev.* **1989**, *18*, 1.
[12] D. C. Duncan, T. L. Netzel, C. L. Hill, *Inorg. Chem.* **1995**, 34, 4640.
[13] C. Streb, K. Kastner, J. Tucher, *Phys. Sci. Rev.* **2019**, *4*, 20170177.
[14] R. S. Quimby, in *Photonics Lasers: An Introduction*, John Wiley & Sons, Inc., Hoboken, NJ, USA, **2006**, pp. 249–279.
[15] O. S. Cifci, A. Kocyigit, P. Sun, *Superlattices Microstruct.* **2018**, *120*, 492.
[16] X. Chen, K. Shehzad, L. Gao, M. Long, H. Guo, S. Qin, X. Wang, F. Wang, Y. Shi, W. Hu, Y. Xu, X. Wang, X. Chen, H. Guo, S. Qin, X. M. Wang, F. Wang, Y. Shi, X. R. Wang, K. Shehzad, Y. Xu, L. Gao, M. Long, W. Hu, *Adv. Mater.* **2020**, *32*, 1902039.
[17] S. Du, W. Lu, A. Ali, P. Zhao, K. Shehzad, H. Guo, L. Ma, X. Liu, X. Pi, P. Wang, H. Fang, Z. Xu, C. Gao, Y. Dan, P. Tan, H. Wang, C.-T. Lin, J. Yang, S. Dong, Z. Cheng, E. Li, W. Yin, J. Luo, B. Yu, T. Hasan, Y. Xu, W. Hu, X. Duan, P. S. Du, W. Lu, et al., *Adv. Mater.* **2017**, *29*, 1700463.
[18] K. Shehzad, T. Shi, A. Qadir, X. Wan, H. Guo, A. Ali, W. Xuan, H. Xu, Z. Gu, X. Peng, J. Xie, L. Sun, Q. He, Z. Xu, C. Gao, Y. S. Rim, Y. Dan, T. Hasan, P. Tan, E. Li, W. Yin, Z. Cheng, B. Yu, Y. Xu, J. Luo, X. Duan, *Adv. Mater. Technol.* **2017**, *2*, 1600262.
[19] F. X. Liang, J. Z. Wang, Z. P. Li, L. B. Luo, *Adv. Opt. Mater.* **2017**, *5*, 1700081.
[20] Y. Zhang, W. Deng, X. Zhang, X. Zhang, X. Zhang, Y. Xing, J. Jie, *ACS Appl. Mater. Interfaces* **2013**, *5*, 12288.
[21] O. Çiçek, S. O. Tan, H. Tecimer, Ş. Altındal, *J. Electron. Mater.* **2018**, *47*, 7134.
[22] H. Kacus, Y. Sahin, S. Aydogan, U. Incekara, M. Yilmaz, M. Biber, *Solid-State Electron.* **2020**, *171*, 107864.
[23] X. Wan, Y. Xu, H. Guo, K. Shehzad, A. Ali, Y. Liu, J. Yang, D. Dai, C. Te Lin, L. Liu, H. C. Cheng, F. Wang, X. Wang, H. Lu, W. Hu, X. Pi, Y. Dan, J. Luo, T. Hasan, X. Duan, X. Li, J. Xu, D. Yang, T. Ren, B. Yu, *npj 2D Mater. Appl.* **2017**, *1*, 1.
[24] E. Yenel, Y. Torlak, A. Kocyigit, İ. Erden, M. Kuş, M. Yıldırım, *J. Mater. Sci.: Mater. Electron.* **2021**, 32, 12094.
[25] M. Laurans, K. Dalla Francesca, F. Volatron, G. Izzet, D. Guerin, D. Vuillaume, S. Lenfant, A. Proust, *Nanoscale* **2018**, *10*, 17156.
[26] N. Li, S. Fang, Z. Sun, R. Liu, L. Xu, *RSC Adv.* **2016**, *6*, 81466.
[27] A. Aouissi, Z. A. Al-Othman, A. Al-Amro, *Int. J. Mol. Sci.* **2010**, *11*, 1343.
[28] S. S. Hosseinyzade, F. M. Zonoz, B. Bahramian, *Catal. Lett.* **2018**, *148*, 1324.
[29] P. Tian, X. He, W. Li, L. Zhao, W. Fang, H. Chen, F. Zhang, W. Zhang, W. Wang, *J. Mater. Sci.* **2018**, *53*, 12016.
[30] C. Sui, R. Yang, R. Yin, J. Gong, C. Shao, L. Qu, *Thin Solid Films* **2008**, *516*, 3899.
[31] K. Fan, H. Chen, B. He, J. Yu, *Chem. Eng. J.* **2020**, *392*, 123744.
[32] L. Zhang, X. Ding, M. Cong, Y. Wang, X. Zhang, *Int. J. Hydrogen Energy* **2019**, *44*, 9203.
[33] J. Arichi, M. M. Pereira, P. M. Esteves, B. Louis, *Solid State Sci.* **2010**, *12*, 1866.
[34] P. B. Koli, K. H. Kapadnis, U. G. Deshpande, M. R. Patil, *J. Nanostruct. Chem.* **2018**, *8*, 453.
[35] J. Zhou, J. Hu, M. Li, H. Li, W. Wang, Y. Liu, R. E. Winans, T. Li, T. Liu, P. Yin, *Mater. Chem. Front.* **2018**, *2*, 2070.

[36] S. Chandra, R. Kumar, *Spectrochim. Acta, Part A* **2005**, *62*, 1050.
[37] O. Basu, S. Mukhopadhyay, S. K. Das, *J. Chem. Sci.* **2018**, *130*, 93.
[38] F. Song, Y. Ding, B. Ma, C. Wang, Q. Wang, X. Du, S. Fu, J. Song, *Energy Environ. Sci.* **2013**, *6*, 1170.
[39] R. Ayranci, Y. Torlak, M. Ak, *J. Electrochem. Soc.* **2019**, *166*, B205.
[40] M. R. Kember, A. J. P. White, C. K. Williams, *Macromolecules* **2010**, *43*, 2291.
[41] J. Luo, N. P. Rath, L. M. Mirica, *Inorg. Chem.* **2011**, *50*, 6152.
[42] P. Kostov, W. Gaberl, H. Zimmermann, *Opt. Laser Technol.* **2013**, *46*, 6.
[43] M. S. Kim, G. J. Lee, H. M. Kim, Y. M. Song, *Sensors* **2017**, *17*, 1774.
[44] C. Xie, C. K. Liu, H. L. Loi, F. Yan, *Adv. Funct. Mater.* **2020**, *30*, 1903907.
[45] Z. Shao, T. Jiang, X. Zhang, X. Zhang, X. Wu, F. Xia, S. Xiong, S. T. Lee, J. Jie, *Nat. Commun.* **2019**, *10*, 1294.
[46] M. Vasilopoulou, E. Polydorou, A. M. Douvas, L. C. Palilis, S. Kennou, P. Argitis, *Energy Environ. Sci.* **2015**, *8*, 2448.
[47] A. Kocyigit, M. Yıldırım, A. Sarılmaz, F. Ozel, *J. Alloys Compd.* **2019**, *780*, 186.
[48] A. Tataroğlu, Ş. Altındal, Y. Azizian-Kalandaragh, *J. Mater. Sci.: Mater. Electron.* **2021**, *32*, 3451.
[49] A. Özmen, S. Aydogan, M. Yilmaz, *Ceram. Int.* **2019**, *45*, 14794.
[50] H. Kacus, Y. Sahin, S. Aydogan, U. Incekara, M. Yilmaz, *J. Sandwich Struct. Mater.* **2021**, *23*, 2547.
[51] O. S. Cifci, M. Bakir, J. L. Meyer, A. Kocyigit, *Mater. Sci. Semicond. Process.* **2018**, *74*, 175.
[52] D. Y. Kim, O. Seok, H. Park, W. Bahng, H. W. Kim, K. C. Park, *Solid-State Electron.* **2018**, *140*, 8.
[53] H. Norde, *J. Appl. Phys.* **1979**, *50*, 5052.
[54] S. K. Cheung, N. W. Cheung, *Appl. Phys. Lett.* **1986**, *49*, 85.
[55] M. Yıldırım, A. Kocyigit, *J. Alloys Compd.* **2018**, *768*, 1064.
[56] M. Yilmaz, A. Kocyigit, B. B. Cirak, H. Kacus, U. Incekara, S. Aydogan, *Mater. Sci. Semicond. Process.* **2020**, *113*, 105039.
[57] M. İlhan, M. M. Koç, B. Coşkun, M. Erkovan, F. Yakuphanoğlu, *J. Mater. Sci.: Mater. Electron.* **2021**, *32*, 2346.
[58] X. Hu, X. Li, G. Li, T. Ji, F. Ai, J. Wu, E. Ha, J. Hu, *Adv. Funct. Mater.* **2021**, 8, 2011284.
[59] D. Kaur, M. Kumar, *Adv. Opt. Mater.* **2021**, *9*, 2002160.
[60] Z. Yang, Y. Deng, X. Zhang, S. Wang, H. Chen, S. Yang, J. Khurgin, N. X. Fang, X. Zhang, R. Ma, *Adv. Mater.* **2018**, *30*, 1704333.
[61] M. Long, P. Wang, H. Fang, W. Hu, *Adv. Funct. Mater.* **2019**, *29*, 1803807.
[62] W. Tian, Y. Wang, L. Chen, L. Li, *Small* **2017**, *13*, 1701848.
[63] M. Xie, W. Chen, Y. na Dong, L. Chen, J. Li, E. Wang, *Dyes Pigm.* **2019**, *166*, 174.
[64] X. Xu, M. Xie, K. Xu, Y. Zhao, *Sol. Energy* **2020**, *209*, 363.
[65] Y. Zheng, X. Xu, F. Li, W. Chen, J. Gong, C. Wang, *Mater. Chem. Front.* **2022**, *6*, 15.
[66] J. Wei, Y. Li, L. Wang, W. Liao, B. Dong, C. Xu, C. Zhu, K. W. Ang, C. W. Qiu, C. Lee, *Nat. Commun.* **2020**, *11*, 6404.
[67] H. Fang, C. Zheng, L. Wu, Y. Li, J. Cai, M. Hu, X. Fang, R. Ma, Q. Wang, H. Wang, *Adv. Funct. Mater.* **2019**, *29*, 1809013.
[68] C. Debiemme-Chouvy, M. C. Bernard, H. Cachet, C. Deslouis, *Surf. Interface Anal.* **2006**, *38*, 531.
[69] Q. Wu, G. Cen, Y. Liu, Z. Ji, W. Mai, *Phys. Lett. Sect. A Gen. At. Solid State Phys.* **2021**, *412*, 127586.
[70] J. Han, C. Fang, M. Yu, J. Cao, K. Huang, *Adv. Electron. Mater.* **2022**, 2100987, https://doi.org/10.1002/aelm.202100987.
[71] C. A. Canbay, O. Karaduman, *J. Mol. Struct.* **2021**, *1235*, 130263.
[72] T. Ouyang, X. Wang, S. Liu, H. Chen, S. Deng, *Front. Mater.* **2021**, *8*, 303.
[73] Z. A. Jezeh, B. Efafi, B. Ghafary, *Sci. Rep.* **2021**, *11*, 15604.
[74] V. Balasubramani, J. Chandrasekaran, V. Manikandan, T. K. Le, R. Marnadu, P. Vivek, *J. Solid State Chem.* **2021**, *301*, 122289.
[75] M. Farbod, R. Taheri, A. Kosarian, *Appl. Mater. Today* **2021**, *24*, 101092.
[76] W. Y. Jiang, Z. Liu, S. Li, Z. Y. Yan, C. L. Lu, P. G. Li, Y. F. Guo, W. H. Tang, *IEEE Sens. J.* **2021**, *21*, 18663.
[77] A. M. El-Mahalawy, K. H. El-Safty, *Optik* **2021**, *246*, 167793.
[78] Y. Zhang, J. Y. Y. Loh, A. G. Flood, C. Mao, G. Sharma, N. P. Kherani, *Adv. Funct. Mater.* **2022**, 2109794, https://doi.org/10.1002/adfm.202109794.
[79] G. Dushaq, M. Rasras, *ACS Appl. Mater. Interfaces* **2021**, *13*, 21499.
[80] Y. Xu, A. Ali, K. Shehzad, N. Meng, M. Xu, Y. Zhang, X. Wang, C. Jin, H. Wang, Y. Guo, Z. Yang, B. Yu, Y. Liu, Q. He, X. Duan, X. Wang, P.-H. Tan, W. Hu, H. Lu, T. Hasan, Y. Xu, A. Ali, K. Shehzad, N. Meng, M. Xu, Z. Yang, T. Hasan, Y. Zhang, X. Wang, C. Jin, et al., *Adv. Mater. Technol.* **2017**, *2*, 1600241.
[81] A. Ali, K. Shehzad, H. Guo, Z. Wang, P. Wang, A. Qadir, W. Hu, T. Ren, B. Yu, Y. Xu, in *Technical Digest – Int. Electron Devices Meeting, IEDM*, Institute of Electrical and Electronics Engineers Inc, Piscataway, NJ **2018**, pp. 8.6.1–8.6.4.